

First Limits on Light Dark Matter Interactions in a Low Threshold Two Channel Athermal Phonon Detector from the TESSERACT Collaboration

C.L. Chang,^{1, 2, 3} Y.-Y. Chang,⁴ L. Chaplinsky,⁵ C.W. Fink,^{4, 6} M. Garcia-Sciveres,^{7, 8} W. Guo,^{9, 10} S.A. Hertel,⁵ X. Li,^{7, *} J. Lin,^{4, 7} M. Lisovenko,¹ R. Mahapatra,¹¹ W. Matava,⁴ D.N. McKinsey,^{4, 7} V. Novati,¹² P.K. Patel,⁵ B. Penning,¹³ H.D. Pinckney,⁵ M. Platt,¹¹ M. Pyle,⁴ Y. Qi,^{9, 10} M. Reed,⁴ G.R.C Rischbieter,¹⁴ R.K. Romani,^{4, †} B. Sadoulet,⁴ B. Serfass,⁴ P. Sorensen,⁷ A. Suzuki,⁷ V. Velan,^{7, ‡} G. Wang,¹ Y. Wang,⁴ S.L. Watkins,⁴ M.R. Williams,^{7, §} and J.K. Wu⁵
 (TESSERACT Collaboration)

T. Aramaki,¹⁵ P. Cushman,¹⁶ N.N. Gite,⁴ A. Gupta,⁴ M.E. Huber,^{17, 18} N.A. Kurinsky,¹⁹ J.S. Mammo,²⁰ A.J. Mayer,²¹ J. Nelson,¹⁶ S.M. Oser,^{21, 22} L. Pandey,²⁰ A. Pradeep,¹⁹ W. Rau,^{21, 23} and T. Saab²⁴

¹Argonne National Laboratory, 9700 S Cass Ave, Lemont, IL 60439, USA

²Kavli Institute for Cosmological Physics, The University of Chicago, Chicago, IL 60637

³Department of Astronomy and Astrophysics, The University of Chicago, Chicago, IL 60637

⁴University of California Berkeley, Department of Physics, Berkeley, CA 94720, USA

⁵University of Massachusetts, Amherst Center for Fundamental

Interactions and Department of Physics, Amherst, MA 01003-9337 USA

⁶Now at Los Alamos National Laboratory, Los Alamos, NM 87545

⁷Lawrence Berkeley National Laboratory, 1 Cyclotron Rd., Berkeley, CA 94720, USA

⁸International Center for Quantum-field Measurement Systems for Studies of the Universe and Particles (QUP), High Energy Accelerator Research Organization (KEK), Oho 1-1, Tsukuba, Ibaraki 305-0801, Japan

⁹Department of Mechanical Engineering, FAMU-FSU College of Engineering,
Florida State University, Tallahassee, FL 32310, USA

¹⁰National High Magnetic Field Laboratory, Tallahassee, FL 32310, USA

¹¹Texas A&M University, Department of Physics and Astronomy, College Station, TX 77843-4242, USA

¹²University of Grenoble Alpes, CNRS, Grenoble INP*, LPSC-IN2P3, 38000 Grenoble, France

¹³University of Zurich, Department of Physics, 8057 Zurich, Switzerland

¹⁴University of Michigan, Randall Laboratory of Physics, Ann Arbor, MI 48109-1040, USA

¹⁵Department of Physics, Northeastern University,
360 Huntington Avenue, Boston, MA 02115, USA

¹⁶School of Physics & Astronomy, University of Minnesota, Minneapolis, MN 55455, USA

¹⁷Department of Physics, University of Colorado Denver, Denver, CO 80217, USA

¹⁸Department of Electrical Engineering, University of Colorado Denver, Denver, CO 80217, USA

¹⁹SLAC National Accelerator Laboratory/Kavli Institute for Particle Astrophysics and Cosmology, Menlo Park, CA 94025, USA

²⁰Department of Physics, University of South Dakota, Vermillion, SD 57069

²¹TRIUMF, Vancouver, BC V6T 2A3, Canada

²²Department of Physics & Astronomy, University of British Columbia, Vancouver, BC V6T 1Z1, Canada

²³Department of Physics, Queen's University, Kingston, Ontario K7L 3N6, Canada

²⁴Department of Physics, University of Florida, Gainesville, FL 32611, USA

(Dated: March 6, 2025)

We present results of a search for spin-independent dark matter-nucleon interactions in a 1 cm^2 by 1 mm thick (0.233 gram) high-resolution silicon athermal phonon detector operated above ground. This sensor achieves an energy resolution of $\sigma_P = 361.5 \pm 0.4 \text{ meV}$, the best for any athermal phonon detector to date. With an exposure of $0.233 \text{ g} \times 12 \text{ hours}$, we place the most stringent constraints on dark matter masses between 44 and $87 \text{ MeV}/c^2$, with the lowest unexplored cross section of $4 \times 10^{-32} \text{ cm}^2$ at $87 \text{ MeV}/c^2$. We employ a conservative salting technique to reach the lowest dark matter mass ever probed via direct detection experiment. This constraint is enabled by two-channel rejection of low-energy backgrounds that are coupled to individual sensors.

I. INTRODUCTION

Current and previous generation dark matter (DM) direct detection experiments such as LZ [1], XENONnT [2], DarkSide [3], and PandaX [4] have largely focused on the detection of weakly interacting massive particles (WIMPs), placing continually tightening constraints on DM models with masses above $1 \text{ GeV}/c^2$. Increasing interest [5–7] in searching for DM below a GeV/c^2 has mo-

* xinranli@lbl.gov

† rkromani@berkeley.edu

‡ vvelan@lbl.gov

§ michaelwilliams@lbl.gov

tivated some collaborations, including CRESST [8, 9], EDELWEISS [10], SuperCDMS [11], and SENSEI [12], to develop experiments sensitive to sub-GeV DM masses. This mass regime contains models of thermal relic DM (e.g. ELDERs [13] and SIMPs [14]), freeze-in DM (e.g. FIMPs [15]), secluded DM [16, 17], Hidden Valleys [18], asymmetric DM [19], and super-symmetric hidden sectors [20, 21] that can either fully or partially produce the correct DM relic abundance. Directly detecting interactions from such DM candidates is challenging, given the sub-keV nuclear recoils they would create in a detector.

Previous efforts to search for sub-GeV nuclear recoils from DM interactions were impeded by an unknown low energy background or backgrounds broadly termed the “Low Energy Excess” (LEE) [22]. These backgrounds are hypothesized to be associated with material effects in the detector environment, such as stress relaxation in the detector holding structure [23] or aluminum sensor films [24], annihilation of radiation-induced defects in the detector crystal [25], or scintillation of materials around the detector [26].

Recently, a subclass of LEE backgrounds has been observed to strongly couple to sensor films from which the detector is constructed [27–29], allowing possible discrimination of this background from DM interactions via a coincidence requirement. Multiple athermal phonon readout channels, coupled to the same detector target, would respond simultaneously to athermal phonon bursts from possible DM signals, while the response to sensor-coupled backgrounds would primarily be confined to a single channel.

In this Letter, we employ this two-channel technique to obtain novel constraints on low-mass DM interactions. This work is part of the TESSERACT (Transition Edge Sensors with Sub-eV Resolution And Cryogenic Targets) initiative, which aims to search for models of sub-GeV DM using a suite of cryogenic detector materials and technologies optimized for low detector thresholds.

II. DETECTOR

We search for low energy DM interactions in a 1 cm^2 by 1 mm thick silicon athermal phonon detector, shown in Fig. 1, which uses voltage-biased tungsten Transition Edge Sensors (TESs [30], $T_c \approx 48\text{ mK}$) coupled to aluminum athermal phonon collection fins in the common Quasiparticle-trap-assisted Electrothermal-feedback Transition edge sensor (“QET”) architecture [31] to sense phonon bursts in the silicon substrate. We wire 50 QETs into two channels of 25 QETs and read out each channel separately with DC SQUID array amplifiers. This readout scheme was designed to discriminate backgrounds which couple primarily to QET metal films from possible DM interactions. These backgrounds were expected to deposit more energy in one readout channel than in the other, whereas DM interactions with the substrate would produce roughly equal responses in both channels.

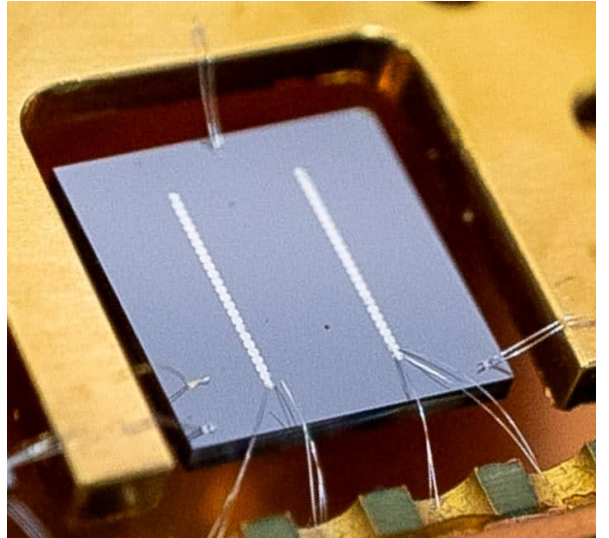


FIG. 1. The TESSERACT 1 cm^2 detector used in this analysis [32]. The detector is supported by wirebonds attached at the top center and bottom corners of the detector. A gold wirebond (left side) is used to cool the detector. The two sensor channels (“left” and “right”) can be seen as the parallel lines, each biased and read out separately (see electrical wire bonds to readout PCB).

Backgrounds associated with stress relaxation in the detector mount were suppressed by suspending the detector by wire bonds as in Ref. [23]. We describe low energy background and noise observations in this detector in Ref. [27].

As we are primarily interested in searching for low energy DM interactions in the detector, we undertook no special precautions to isolate our detector from high-energy backgrounds (e.g. background radioactivity, cosmic rays). We operated our detector in a dilution refrigerator two floors below ground level at the University of California, Berkeley.

To calibrate our detector’s response, we injected short ($\sim\mu\text{s}$) pulses of small numbers of 3.06 eV photons onto the detector, creating an athermal pulse of quantized energy [27]. By observing the responses in the two channels, we measure the expected pulse shape for phonon DM-like events, and by combining the responses in the two channels measure a world-leading baseline phonon energy resolution of $\sigma_P = 361.5 \pm 0.4\text{ meV (stat.)}$.

Current signals from the two detector channels were continuously digitized at 1.25 MHz. Twenty-four hours of data were collected, interleaved with periods where the detector state was monitored to ensure stable operation. To mitigate bias in the analysis, the dataset was divided into 96 15-minute periods. Odd-numbered periods were unblinded and used to develop the analysis pipeline. Even-numbered periods were kept blinded and only opened after the analysis was finalized. Results from the blinded dataset are presented here.

III. OFFLINE TRIGGER AND MULTI-CHANNEL OPTIMAL FILTERING

Offline analysis is performed in two stages: triggering, in which event times are identified, and feature extraction, in which event amplitudes are measured. Both stages use Optimum (Matched) Filtering [33, 34], a class of algorithms designed to identify small signal pulses in a noisy data stream.

A. Building an Optimal Filter

An Optimal Filter (OF) requires two elements: noise and signal models. The noise is assumed to be stationary (time-independent) and Gaussian-distributed at each frequency, and is obtained by calculating the average N -channel cross-spectral density (CSD) for signal-free waveforms. To model the signal, we exploit the fact that for unsaturated energy depositions, the normalized pulse shape is independent of energy [30, 34, 35]. The pulse response is determined by the TES's electrical and thermal couplings to its environment, as well as the detector's athermal phonon collection dynamics and efficiency. We study our detector's response to real energy depositions (backgrounds and calibration photons), and characterize our TESSs' electrothermal response [29, 34, 35], allowing us to develop signal templates, gain insight into the underlying phonon collection dynamics for different event classes, and calibrate the energy deposition scale.

Combining the signal and noise models into a χ^2 estimator and minimizing χ^2 for an observed current trace, the OF identifies the best-fit signal amplitudes and pulse start times. This procedure is *optimal*; it allows us to identify and estimate energy depositions down to the lowest possible threshold (see Appendix A).

An OF can be used to fit the simultaneous response in N readout channels with channel-specific pulse shapes scaled by M independent amplitudes in an " $N \times M$ " Optimal Filter. Each of the M templates contains N channel-specific pulse shapes, whose amplitudes change together. Consider an OF with $N = 2$ and $M = 1$ where the sole signal template contains two pulse shapes, one per channel. For $M = 1$, the OF only contains one *amplitude degree of freedom*. The pulses in both channels may rise or fall depending on the energy deposited, but they do so together; the ratio of pulse heights between channels is fixed. We can set either pulse shape in this template to a constant-zero waveform—an expectation that the signal manifests in a single channel, but the noise can be subtracted using both channels. In contrast, we could construct a 2×2 OF using two templates. Template A could contain two pulse shapes: a waveform in Channel A with the desired pulse shape, and a constant-zero waveform in Channel B. Similarly, Template B could contain two pulse shapes: the same as A, but in reverse. This strategy allows the amplitudes of the pulses in both channels to float independently, while the pulses remain

simultaneous in time.

For each amplitude A_α in an $N \times M$ OF, we reconstruct the energy absorbed in Si substrate phonons through a linear transformation, where the coefficient is empirically determined with the optical photon calibration:

$$E_{\text{reconstructed}, \alpha} = k_\alpha A_\alpha . \quad (1)$$

B. Implementing NxM Optimal Filters

We observe two classes of signal shapes, described in detail in Ref. [27]: 1) a "shared" ("phonon-like") shape that represents energy simultaneously deposited in both readout channels and is consistent with photon calibration events and DM interactions with the substrate; 2) a "singles" shape that represents backgrounds coupled primarily to a single sensor channel. Both the shared and singles template shapes are empirically derived from background data. The average shared and singles pulse shapes are visible in the inserts of Fig. 2.

We expect a DM-induced nuclear recoil to create a phonon pulse in the silicon target, generating coincident responses in the two readout channels as observed in calibration events [27]. Thus, we trigger on the amplitude of a 2×1 OF, using the shared signal shapes as our template, implicitly assuming that the phonon signals in both channels can be scaled by the same amplitude. Events are triggered when this amplitude exceeds $4\sigma_{\text{noise}}$, corresponding to 1.45 ± 0.02 eV; σ_{noise} is the baseline sensor noise. Continuous periods of time when the OF amplitude exceeds the trigger threshold are assembled into discrete events, using a maximum window of 2 ms. More details about the trigger can be found in Appendix A.

To extract data features, two types of optimal filters are deployed on each triggered event. First, we inspect energy partitioning between the two readout channels by fitting a 2×2 OF to each event, allowing the best-fit amplitude (i.e., energy) in each channel to vary independently.

Second, to discriminate potential DM signals (shared events) from background events (singles), we fit three 2×1 OFs to each event. We assume shared phonons, left channel singles, and right channel singles event topologies, respectively. In this way, each event is associated with three best-fit χ^2 values: χ^2_{shared} , $\chi^2_{\text{singleLeft}}$, and $\chi^2_{\text{singleRight}}$. To compare these signal template assumptions, we further define

$$\delta\chi^2_{SL} = \chi^2_{\text{shared}} - \chi^2_{\text{singleLeft}} \quad (2)$$

$$\delta\chi^2_{SR} = \chi^2_{\text{shared}} - \chi^2_{\text{singleRight}} \quad (3)$$

$$\delta\chi^2_{LR} = \chi^2_{\text{singleLeft}} - \chi^2_{\text{singleRight}} . \quad (4)$$

For example, an event with $\delta\chi^2_{SL} > 0$ is more consistent with a singles pulse in the left channel than with a shared pulse, and $\delta\chi^2_{LR} < 0$ is more consistent with a left singles event than a right singles event.

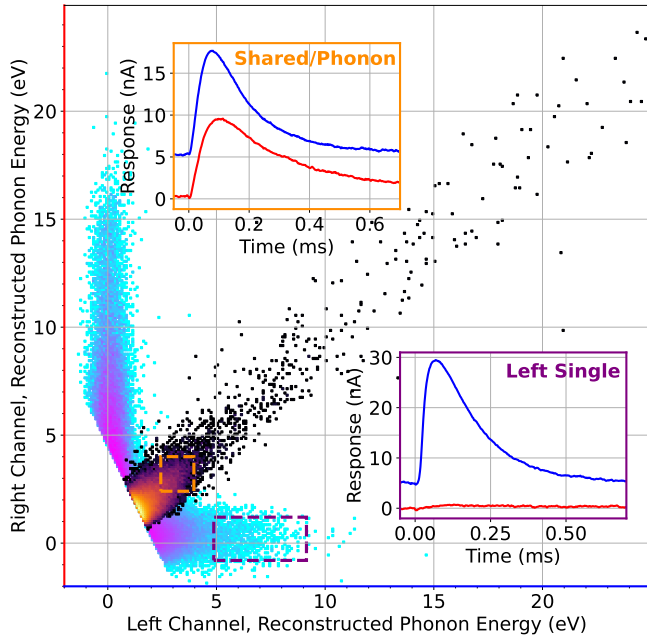


FIG. 2. **(Main)** Two dimensional histogram of observed events. Black to orange points on the diagonal show accepted shared/phonon events; blue to purple points show singles events which are inconsistent with a DM response and excluded in the DM search. For energy reconstruction, we assume a phonon pulse shape and correct for phonon collection efficiency, leading left and right singles events to be reconstructed at 15.6 and 28.2 times the energy they deposit in the corresponding channels (on average). Singles and shared events are discriminated using $\delta\chi^2$; see text. **(Top Left Insert)** Averaged shared/phonon event response in the left (blue) and right (red) channels for events in orange dashed box in main figure. **(Bottom Right Insert)** Averaged left singles event response in the left (blue) and right (red) channels for events in purple dashed box in main figure. In both insert figures, traces are offset and low pass filtered at 50 kHz for clarity.

After applying these OFs, the distribution of triggered event energies is plotted in Fig. 2. Reconstructed energies are measured with the 2×2 OF. The histogram is colored based on the three 2×1 OFs—the black-orange heat map represents shared-like events ($\delta\chi^2_{SL} < 0$ and $\delta\chi^2_{SR} < 0$), and the blue-purple heat map represents other events. We observe that the events divide into three primary populations: shared events consistent with calibrations and DM, on the $x \approx y$ diagonal; left and right channel singles, on the x and y axes. Figure 3 depicts two example measured events, compared with best-fit shared and singles templates.

IV. EVENT SELECTION AND EFFICIENCIES

Our trigger finds 434,090 events, each reconstructed with a trace length of 20 ms. To remove events in peri-

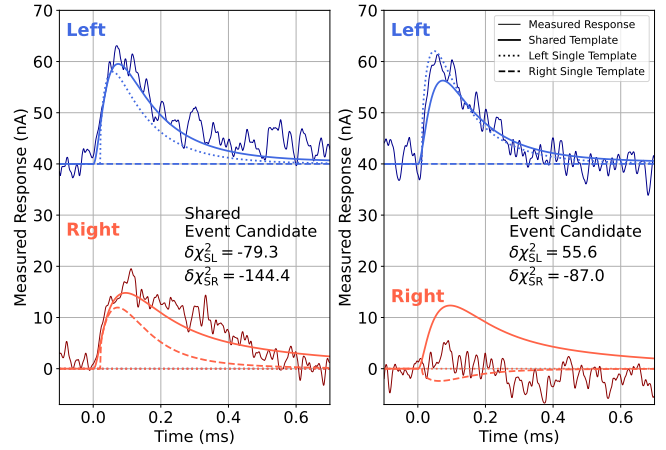


FIG. 3. A candidate shared event (left panel) and a candidate left singles event (right panel) observed in our detector. We compare the measured response (thin solid line) with three templates: a shared response in both channels (thick solid line), a left singles (dotted), and a right singles (dashed) in the left and right channels, respectively. By using $\delta\chi^2$ statistics, we can determine whether the shape and amplitude in both channels are most consistent with a shared, left singles, or right singles event. Data is filtered with a 50 kHz low-pass filter and offset for clarity. Left and right events have reconstructed energies of 4.97 and 3.31 eV respectively using a shared template.

ods of poor data quality where the detector response will be abnormal (e.g. periods of high electromagnetic interference (EMI) or vibration induced noise, or “pileup” events with multiple triggers in the same OF window), we impose data quality cuts. To reject periods of high EMI or noise, as well as elevated detector temperature following e.g. high-energy cosmic ray interactions, we cut events where the pre-pulse quiescent current (baseline) or difference between pre- and post-pulse currents (slope) fell outside a predetermined range from the unblinded dataset. These cuts remove 4.5 % of events. We additionally perform a cut based on the χ^2 value extracted from the OF for every given pulse (considering only frequencies below 50 kHz and assuming a phonon template), rejecting events which are inconsistent with the expected pulse shape. This 5.6σ low frequency χ^2 cut has the effect of removing pileup, triggers at incorrect times, and events with high noise or abnormal pulse shape. Events passing these cuts in both of our detector channels are preliminarily accepted as DM candidate events.

To reject backgrounds which couple primarily to the phonon sensors, we perform a final selection of events with $\delta\chi^2_{SL} < 0$ and $\delta\chi^2_{SR} < 0$ (i.e. events that are more shared-like than singles-like). Events which pass this additional $\delta\chi^2$ cut are accepted into our final DM analysis. We lastly place an analysis threshold of 1.5 eV, removing any events below this energy. The final event spectrum can be seen in Fig. 4.

We measure the impact of these cuts on the detector

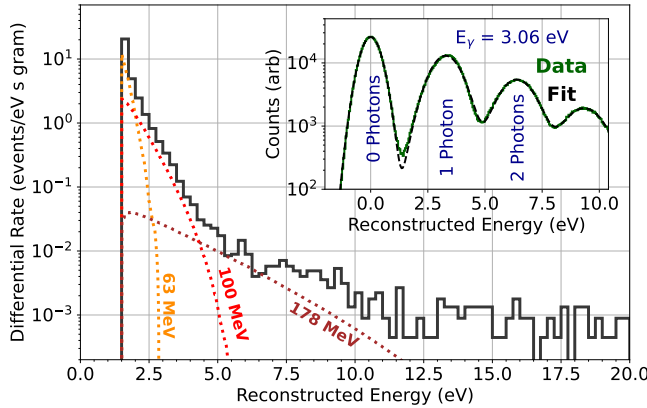


FIG. 4. (Main) Spectrum of observed events passing quality cuts and shared event cuts (black). Dotted lines show the modeled DM interaction spectra at the limit of exclusion for DM with masses 63, 100, and 178 MeV/c². (Inset) Calibration spectrum, showing peaks from absorbing zero, one, two, etc. photons.

nuclear recoil (NR) efficiency using injected virtual pulses with an ideal shared pulse shape (“salt”) [36]. Salt pulses at a range of NR energies, as low as 0.361 eV, are injected into the continuous data stream pre-trigger. For each injected energy, we measure the binned difference between the salted and unsalted spectrum and normalize by the total number of salts. This net differential signal response estimates inefficiencies due to triggering, analysis cuts, and measures energy smearing. The response to sub-threshold recoil energies observed through *noise boosting* [36] is also studied provided that the signal response is linear and has small true signal pileup. See Appendix B for details. This is convolved with the standard spin-independent NR DM spectrum dR/dE [37] to build the model of measured spectrum dR/dE' . The dR/dE' spectra for DM masses of 63, 100, and 178 MeV/c² can be seen overlaid on the measured event spectrum in Fig. 4.

V. RESULTS

The total exposure is $0.233\text{ g} \times 12\text{ h}$. The interaction rate between DM and silicon nuclei is modeled assuming scattering from DM with a local density of 0.3 GeV/cm^3 and a Maxwell–Boltzmann velocity distribution, using the parametrization of Lewin and Smith [37]. This model is convolved with the detector net differential sensitivity estimated via salting to get the net differential response for a given DM model [36].

The limit on the DM-nucleon spin-independent scattering cross-section σ_{SI} is calculated with the Yellin optimum interval method [38, 39] at the 90 % confidence level, using reconstructed energy as the only observable. The background is completely un-modeled and is thus considered potential DM signal. As is standard for DM searches at relatively high cross-sections [11, 40], we take

into consideration the shielding effect from the overburden. This includes the atmosphere and 3 m concrete floors above the lab, and is calculated using the *Verne* code base [41, 42]. The resulting limit given this overburden consideration is seen as the blue dashed line in Fig. 5.

Some of this nominally excluded parameter space has a DM interaction rate that would lead to significant signal pileup. In this regime, the dR/dE' does not scale linearly with σ_{SI} , rendering any linear interaction model incorrect [36]. To account for this, we further restrict the exclusion region to include only DM masses and cross-sections that would not produce significant pileup. To estimate the rate at which we begin to see pileup effects, we note that $91\text{ }\mu\text{s}$ after a phonon pulse is triggered, the OF will relax to 10% of its peak amplitude. This suggests that a pileup rate of $1/(2 \times 91\text{ }\mu\text{s}) = 5.5\text{ kHz}$ is a reasonable upper exclusion boundary, below which our linear differential rate modeling is valid. This is seen as the red dotted curve in Fig. 5. Future analyses can be designed specifically to search for DM with high pileup rates. These analyses will likely extend the reaches of this detector and others to substantially lower DM masses and higher interaction cross sections [43, 44].

New bounds on cross sections as low as $4 \times 10^{-32}\text{ cm}^2$ below 87 MeV/c² DM mass are established. We place constraints on DM-nucleon cross sections down to masses of 44 MeV/c² at $4.67 \times 10^{-30}\text{ cm}^2$, the lowest mass ever probed by a particle-like DM search, as a consequence of our excellent energy resolution. We place our most stringent bounds for DM with a cross-section of $6.56 \times 10^{-35}\text{ cm}^2$ at 500 MeV/c². The full DM exclusion region from this work can be seen as the blue shaded region in Fig. 5.

VI. CONCLUSION

This letter presents the lowest-mass sensitivity of any dark matter nuclear recoil search, as a result of our unparalleled energy resolution of $361.5 \pm 0.4\text{ meV}$. By treating our unknown background with the optimum interval, we are able to place world-leading constraints on DM between 44 MeV/c² and 87 MeV/c². These results show the potential of low-threshold superconducting sensors for exploring new DM parameter space. Through both the direct minimization of low energy excess backgrounds and the discrimination of these backgrounds with novel cryogenic targets like gallium arsenide and superfluid He [45, 46], TESSERACT aims to substantially improve upon this surface DM search, as well as search for other DM interactions.

ACKNOWLEDGMENTS

The athermal phonon detector used in this search builds upon the work that has been done by the CDMS

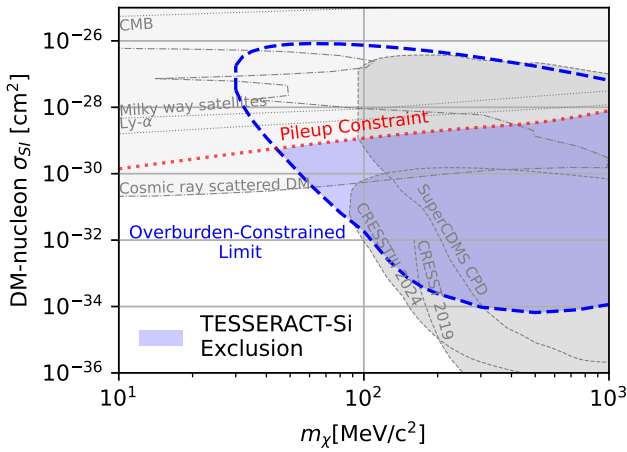


FIG. 5. The 90 % C.L. limits on spin-independent DM below 1 GeV/c². The blue shaded region shows the exclusion from this work. The blue dashes line represents the exclusion from the Yellin optimum interval test when considering the effect of the overburden. The red dotted line is from the requirement that there be no DM signal pileup. Previously excluded DM phase space from the CRESST [8, 40] and SuperCDMS [11] collaborations are shown in gray. Constraints from cosmology and astrophysics are shown in light gray [47–51].

and SuperCDMS collaborations [31, 52, 53]. This work was supported in part by DOE Grants DE-SC0022916, DE-SC0019319, DE-SC0025523 and DOE Quantum Information Science Enabled Discovery (QuantISED) for High Energy Physics (KA2401032) and National Science Foundation Grants 2111375 and 1106400. This material is based upon work supported by the Department of Energy National Nuclear Security Administration through the Nuclear Science and Security Consortium under Award Number(s) DE-NA0003180 and/or DE-NA0000979. Work at Lawrence Berkeley National Laboratory was supported by the U.S. DOE, Office of High Energy Physics, under Contract No. DEAC02-05CH11231. Work at Argonne is supported by the U.S. DOE, Office of High Energy Physics, under Contract No. DE-AC02-06CH11357. Work at Texas A&M University was supported by the Mitchell Institute and by the U.S. DOE, Office of High Energy Physics, under Contract Nos. DE-SC0018981 and DE-SC0021051. W.G. and Y.Q. acknowledge the support by the National High Magnetic Field Laboratory at Florida State University, which is supported by the National Science Foundation Cooperative Agreement No. DMR-2128556 and the state of Florida.

Appendix A: Multi-Channel Optimal Filtering

Our offline analysis trigger extends the Optimal (Matched) Filter algorithm [33, 34] to N simultaneous readout channels and M potential signal shapes. It is

based on $\chi_s^2(\vec{A}, t)$, defined below, which represents the consistency of an observed trace with one or more signal templates labeled by s .

$$\begin{aligned} \chi_s^2(\vec{A}, t) &\equiv \int df \chi_s^2(\vec{A}, t, f) , \\ \text{and } \chi_s^2(\vec{A}, t, f) &\equiv \\ &\sum_{i,j=1}^{N,N} \left(v_i^* - \sum_{\alpha=1}^M A_{\alpha} e^{i\omega t} s_{i\alpha}^* \right) C_{ij}^{-1} \left(v_j - \sum_{\beta=1}^M A_{\beta} e^{-i\omega t} s_{j\beta} \right). \end{aligned} \quad (\text{A1})$$

Here, $s_{i\alpha}$ is the Fourier transform of signal template α in each readout channel i ; v_i the Fourier transform of the observed trace in channel i ; C_{ij} is the cross-spectral density between channels i and j ; \vec{A} is an M -length vector of signal template amplitudes; and we integrate over frequencies $f \equiv \omega/2\pi$. Due to discrete time sampling, the integral becomes a sum over frequencies between $-f_{\text{samp}}/2$ and $f_{\text{samp}}/2$ in steps of $1/T$, where f_{samp} is the sampling frequency and T is the trace time length—1.25 MHz and 20 ms, respectively, in this study.

We then construct $\Delta\chi_s^2(t)$ as below, where \hat{A} is the value of \vec{A} that minimizes $\chi_s^2(\vec{A}, t)$:

$$\Delta\chi_s^2(t) \equiv \chi_s^2(0, t) - \chi_s^2(\hat{A}, t) \quad (\text{A2})$$

This represents, for a given trace, the difference between the minimal χ^2 and the χ^2 that would be obtained by assuming no signal¹. Our $N \times M$ Optimal Filter trigger runs on $\Delta\chi_s^2(t)$, optimally selecting pulses that cross a certain threshold. This allows us to cleanly vary the signal template without changing the trigger parameters. It can be shown that $\Delta\chi_s^2(t)$ is quadratically dependent on the best-fit signal amplitude \hat{A} . For the simple case of one readout channel and one signal template, this trigger is thus identical to triggering on the Optimal Filter amplitude, as described in [34].

This trigger is applied to the data, using a 2×1 shared template that considers a simultaneous pulse in both channels $\Delta\chi_{\text{shared}}^2$. Events are selected when $\Delta\chi_{\text{shared}}^2$ exceeds 16, or equivalently when the best-fit amplitude \hat{A} exceeds $4\sigma_{\text{base}}$. Here, σ_{base} is the baseline resolution of \hat{A} , i.e. the magnitude of fluctuations of \hat{A} due only to noise.

For a given pulse, $\Delta\chi_{\text{shared}}^2$ will exceed the trigger threshold continuously for some amount of time, so we select triggers by assembling above-threshold regions of time within a 2-ms window into discrete events. This window was selected to capture all unsaturated signals while minimizing deadtime. Within each region, the trigger is placed at the time that maximizes $\Delta\chi_{\text{shared}}^2$.

¹ Note that $\Delta\chi^2$ is different than $\delta\chi^2$, defined in the main text.

Appendix B: Noise modeling with the Salting Method

The upward fluctuation of noise allows additional sensitivity to events with sub-threshold true energies that are boosted above the trigger threshold. This idea has been widely adopted in DM searches [8, 11]. The upward fluctuation is usually limited to 3σ of the baseline energy resolution to prevent sensitivities to zero energy events. Discussions in [36] pointed out that a more rigorous modeling of the noise smearing the true event energy without the arbitrary 3σ cut-off can be achieved by salting the raw data traces with ideal signal pulses.

The core concept is the net differential response, defined as

$$\Delta f(E'|E) \equiv f(E'|E) - f(E'|0) \quad (\text{B1})$$

where E is the true energy and E' is the measured energy. The quantity $f(E'|E)$ represents the probability distribution of E' given that events with energy E are present. The $-f(E'|0)$ term accounts for the reduction of noise-only time periods in the measurement as signals are added. In previous works, this term is ignored because the overlap between $f(E'|E)$ and $f(E'|0)$ above the trigger threshold is negligible. However, it is problematic if signals with $E \sim 0$ are considered, resulting in underestimation of DM cross sections at low-masses.

We estimate $\Delta f(E'|E)$ using the salting method. First, N_s pulses (salts) with ideal signal pulse shape and

energy E_s are injected into the continuously recorded raw traces of total exposure time T randomly in time. The random injection times are separated by the triggered trace length to prevent pileup of two salt pulses. Second, the salted traces are processed by the offline trigger and filtering algorithm as described in Sec. III, then selected under the same criteria as in Sec. IV. The exact same analysis is done for both salted and unsalted datasets to ensure the accurate measurement of trigger and event selection efficiencies. Then, the measured spectrum $\widehat{\frac{dR}{dE'}}(E'|S+s)$ is compared with the one before salting $\widehat{\frac{dR}{dE'}}(E'|S)$, and normalized by $r_s = N_s/T$ to estimate $\Delta f(E'|E)$

$$\widehat{\Delta f}(E'|S+E_s) = \frac{\widehat{\frac{dR}{dE'}}(E'|S+s) - \widehat{\frac{dR}{dE'}}(E'|S)}{r_s} \quad (\text{B2})$$

where S represent the potential DM signal in the unsalted spectrum, and s represents the salt. Finally, salting is repeated at energies from 0.361 eV to 30 eV. The limit of DM with mass m_χ is calculated with the Yellin optimum interval method [39], with

$$\begin{aligned} & \Delta \frac{dR}{dE'}(E'|S, s(m_\chi, \sigma_0)) \\ & \equiv \int_0^\infty \frac{dR}{dE'}(E_s | s(m_\chi, \sigma_0)) \widehat{\Delta f}(E'|S+E_s) dE_s \end{aligned} \quad (\text{B3})$$

scaling with σ_{SI} but not $\frac{dR}{dE'}$. Here σ_0 is the reference DM cross section. See [36] for full discussion.

-
- [1] D. S. Akerib *et al.* (LZ Collaboration), Nucl. Instrum. Meth. A **953**, 163047 (2020), arXiv:1910.09124 [physics.ins-det].
- [2] E. Aprile *et al.* (XENON Collaboration), Phys. Rev. Lett. **131**, 041003 (2023), arXiv:2303.14729 [hep-ex].
- [3] P. Agnes *et al.* (DarkSide-50), Phys. Rev. D **107**, 063001 (2023), arXiv:2207.11966 [hep-ex].
- [4] Y. Meng *et al.* (PandaX-4T Collaboration), Phys. Rev. Lett. **127**, 261802 (2021), arXiv:2107.13438 [hep-ex].
- [5] Y. Hochberg, E. Kuflik, T. Volansky, and J. G. Wacker, Physical Review Letters **113**, 171301 (2014).
- [6] Y. Hochberg, E. Kuflik, H. Murayama, T. Volansky, and J. G. Wacker, Physical Review Letters **115**, 021301 (2015).
- [7] E. Kuflik, M. Perelstein, N. R.-L. Lorier, and Y.-D. Tsai, Journal of High Energy Physics **2017**, 78 (2017).
- [8] A. H. Abdelhameed *et al.* (CRESST), Phys. Rev. D **100**, 102002 (2019), arXiv:1904.00498 [astro-ph.CO].
- [9] G. Angloher *et al.* (CRESST), Phys. Rev. D **107**, 122003 (2023), arXiv:2212.12513 [astro-ph.CO].
- [10] E. Armengaud *et al.* (EDELWEISS), Phys. Rev. D **99**, 082003 (2019), arXiv:1901.03588 [astro-ph.GA].
- [11] I. Alkhateeb *et al.* (SuperCDMS), Phys. Rev. Lett. **127**, 061801 (2021), arXiv:2007.14289 [hep-ex].
- [12] O. Abramoff *et al.* (SENSEI), Phys. Rev. Lett. **122**, 161801 (2019), arXiv:1901.10478 [hep-ex].
- [13] E. Kuflik, M. Perelstein, N. R.-L. Lorier, and Y.-D. Tsai, Phys. Rev. Lett. **116**, 221302 (2016), arXiv:1512.04545 [hep-ph].
- [14] Y. Hochberg, E. Kuflik, T. Volansky, and J. G. Wacker, Phys. Rev. Lett. **113**, 171301 (2014).
- [15] L. J. Hall, K. Jedamzik, J. March-Russell, and S. M. West, JHEP **03**, 080 (2010), arXiv:0911.1120 [hep-ph].
- [16] C. Boehm and P. Fayet, Nucl. Phys. B **683**, 219 (2004), arXiv:hep-ph/0305261.
- [17] M. Pospelov, A. Ritz, and M. Voloshin, Physics Letters B **662**, 53 (2008).
- [18] M. J. Strassler and K. M. Zurek, Physics Letters B **651**, 374 (2007).
- [19] D. E. Kaplan, M. A. Luty, and K. M. Zurek, Phys. Rev. D **79**, 115016 (2009).
- [20] J. L. Feng and J. Kumar, Phys. Rev. Lett. **101**, 231301 (2008).
- [21] D. Hooper and K. M. Zurek, Physical Review D **77** (2008), 10.1103/physrevd.77.087302.
- [22] P. Adari *et al.*, SciPost Physics Proceedings , 001 (2022).
- [23] R. Anthony-Petersen *et al.*, Nature Communications **15** (2024), 10.1038/s41467-024-50173-8.
- [24] R. K. Romani, Journal of Applied Physics **136** (2024), 10.1063/5.0222654.
- [25] K. Nordlund, F. Kong, F. Djurabekova, M. Heikinheimo, K. Tuominen, and N. Mirabolafathi, “Defect recombination

- tion origin of low energy excess in semiconductor detectors,” (2024).
- [26] P. Du, D. Egana-Ugrinovic, R. Essig, and M. Sholapurkar, Phys. Rev. X **12**, 011009 (2022).
- [27] R. Anthony-Petersen *et al.*, “Low energy backgrounds and excess noise in a two-channel low-threshold calorimeter,” (2024).
- [28] G. Angloher *et al.*, “Doublets detectors to investigate the cresst low energy background: results from above-ground prototypes,” (2024).
- [29] R. K. Romani, Y.-Y. Chang, R. Mahapatra, M. Platt, M. Reed, I. Rydstrom, B. Sadoulet, B. Serfass, and M. Pyle, “A transition edge sensor operated in coincidence with a high sensitivity phonon veto for photon coupled rare event searches,” (2024).
- [30] K. D. Irwin, Applied Physics Letters **66**, 1998–2000 (1995).
- [31] K. D. Irwin, S. W. Nam, B. Cabrera, B. Chugg, and B. A. Young, Review of Scientific Instruments **66**, 5322 (1995).
- [32] Photo courtesy of Marilyn Sargent/Lawrence Berkeley National Laboratory.
- [33] S. R. Golwala, *Exclusion limits on the WIMP nucleon elastic scattering cross-section from the Cryogenic Dark Matter Search*, Ph.D. thesis, UC, Berkeley (2000).
- [34] S. L. Watkins, *Athermal Phonon Sensors in Searches for Light Dark Matter*, Ph.D. thesis, UC, Berkeley (main) (2022), arXiv:2301.08699 [hep-ex].
- [35] K. Irwin and G. Hilton, in *Cryogenic Particle Detection*, Topics in Applied Physics, edited by C. Enss (Springer, Berlin, Heidelberg, 2005) pp. 63–150.
- [36] X. Li, M. Pyle, and B. Sadoulet, “Modeling the differential rate for signal interactions in coincidence with noise fluctuations or large rate backgrounds,” (2024), arXiv:2411.10671 [hep-ex].
- [37] J. Lewin and P. Smith, Astropart. Phys. **6**, 87 (1996).
- [38] S. Yellin, Phys. Rev. D **66**, 032005 (2002), arXiv:physics/0203002.
- [39] S. Yellin, (2008), arXiv:0709.2701 [physics.data-an].
- [40] G. Angloher *et al.* (CRESST), Phys. Rev. D **110**, 083038 (2024), arXiv:2405.06527 [astro-ph.CO].
- [41] B. J. Kavanagh, Phys. Rev. D **97**, 123013 (2018), arXiv:1712.04901 [hep-ph].
- [42] B. J. Kavanagh, “bradkav/verne: Version 2.0,” (2024).
- [43] A. Das, N. Kurinsky, and R. K. Leane, Phys. Rev. Lett. **132**, 121801 (2024), arXiv:2210.09313 [hep-ph].
- [44] work in progress, “Constrain dark matter interactions with noise power.”.
- [45] S. A. Hertel, A. Biekert, J. Lin, V. Velan, and D. N. McKinsey, Phys. Rev. D **100**, 092007 (2019).
- [46] R. Anthony-Petersen *et al.* (SPICE, HeRALD), Phys. Rev. D **110**, 072006 (2024), arXiv:2307.11877 [physics.ins-det].
- [47] C. V. Cappiello and J. F. Beacom, Phys. Rev. D **100**, 103011 (2019), [Erratum: Phys. Rev. D 104, 069901 (2021)], arXiv:1906.11283 [hep-ph].
- [48] T. Bringmann and M. Pospelov, Phys. Rev. Lett. **122**, 171801 (2019), arXiv:1810.10543 [hep-ph].
- [49] E. O. Nadler *et al.* (DES), Phys. Rev. Lett. **126**, 091101 (2021), arXiv:2008.00022 [astro-ph.CO].
- [50] K. K. Rogers, C. Dvorkin, and H. V. Peiris, Phys. Rev. Lett. **128**, 171301 (2022).
- [51] V. Gluscevic and K. K. Boddy, Phys. Rev. Lett. **121**, 081301 (2018).
- [52] J. Yen *et al.*, Applied Physics Letters **105**, 163504 (2014), <http://dx.doi.org/10.1063/1.4899130>.
- [53] M. C. Pyle, *Optimizing the design and analysis of cryogenic semiconductor dark matter detectors for maximum sensitivity*, Ph.D. thesis, Stanford U. (2012).